Available online at www.sciencedirect.com

jmr&t Journal of Materials Research and Technology

journal homepage: www.elsevier.com/locate/jmrt

Original Article

Development of novel hybrid TPMS cellular lattices and their mechanical characterisation

Nejc Novak [a,*], Oraib Al-Ketan [b,**], Matej Borovinšek [a], Lovre Krstulović-Opara [c], Reza Rowshan [b], Matej Vesenjak [a], Zoran Ren [a]

[a] Faculty of Mechanical Engineering, University of Maribor, Maribor, Slovenia
[b] Core Technology Platforms Operations, New York University Abu Dhabi, Abu Dhabi, United Arab Emirates
[c] Faculty of Electrical Engineering, Mechanical Engineering and Naval Architecture, University of Split, Split, Croatia

ARTICLE INFO

Article history:
Received 26 July 2021
Accepted 23 August 2021
Available online 28 August 2021

Keywords:
Cellular materials
Triply periodical minimal surface
Hybrid lattices
Experimental testing
Computational modelling
Multi-morphology

ABSTRACT

Uniform lattices composed of one type of lattice structure repeated periodically have been extensively investigated in literature for their mechanical and physical properties. Their promising properties, which include a desirable combination of high strength, stiffness and toughness, suggest that hybrid structures made of two or more lattice types can exhibit even more advantageous and desired properties. In this work, the mechanical properties of hybrid cellular structures designed using implicit functions are investigated both experimentally and numerically. Two proposed samples are investigated comprised of a Gyroid and a Diamond unit cells hybridised linearly and radially. First, a finite element computational model was utilised in LS-DYNA to capture the mechanical properties of the additively manufactured constituent lattices (i.e., Gyroid and Diamond) made of stainless steel 316L and tested under dynamic and quasi-static loading conditions. The model was validated for three different relative densities. Then, the validated computational model was then tested to predict the mechanical behaviour of the proposed hybrid lattices. Finally, the proposed hybrid lattices were fabricated and mechanically tested to obtain their mechanical properties. A good agreement between experimental and computational results was achieved. The validated computational models will be used to evaluate other designs of TPMS lattices and their crashworthiness performance for protective equipment applications.

1. Introduction

Cellular structures are being comprehensively investigated regarding their mechanical and physical properties for use in modern applications, e.g. technology, medicine, fashion, and other areas [1,2]. They are one of the most promising building materials for future products due to their attractive combination of lightweight properties, high energy absorption capacity, damping and thermal insulation [3,4]. The use of cellular materials in functional components is growing increasingly due to significant advances in manufacturing processes and the lowering of fabrication costs [3].

* Corresponding author.
** Corresponding author.
E-mail addresses: n.novak@um.si (N. Novak), oraib.alketan@nyu.edu (O. Al-Ketan).
https://doi.org/10.1016/j.jmrt.2021.08.092

The development and fabrication of periodic cellular structures, commonly known as lattices, has been made possible by recent advances in additive manufacturing [5]. Regular lattices are simple to design using computer-aided design software, and their behaviour under loading is easier predictable because of their periodicity. The behaviour of several types of strut-based unit cells under quasi-static and dynamic loading has been thoroughly studied [6–8]. Some new types of periodic closed-cell lattices have been developed and mechanically characterised recently. Examples include the plate-type lattices [9–11] and the shell-based triply periodic minimal surface (TPMS) lattices designed based on implicit functions [12–17]. While plate-type lattices demonstrated desirable properties with stiffness values that may reach the Hashin-Shtrikman upper bounds in low relative densities, their closed-cell topology mandates adding additional holes for resin or powder removal in AM process which may deteriorate their properties due to stress concentration. On the other hand, TPMS-based lattices are partially open lattices with an interconnected network of pores that allows easy removal of resin and powder. Al-Ketan et al. [7] showed that the sheet-based TPMS structures exhibit enhanced mechanical properties compared to the strut-based TPMS lattices and other standard strut-based lattices, such as the octet-truss and the Kelvin unit cells due to the contribution of cell wall stretching. Other lattices have also been derived from TPMS lattices, such as functionally graded TPMS lattices [18] and honeycomb Gyroid [19]. While uniform lattices composed of one type of lattice structure repeated periodically have been extensively investigated in literature for their mechanical and physical properties, their promising properties suggest that hybrid structures made of two or more lattice types can exhibit even more advantageous and desired properties. This was indeed the focus of several recent studies [20–23]. For example, Alberdi et al. [20] investigated multi-morphology lattices composed using FCC and BCC unit cells and showed improved plastic energy absorption under quasi-static compressive loading as compared to the individual unit cells. Moreover, they showed that a rational design approach could inspire multi-morphology lattices which exceed rule-of-mixtures expectations. Chen et al. [22] built on the fact that certain TPMS lattices exhibit high Young's modulus on the expense of shear modulus and vice versa to propose hybrid structures combining the different TPMS. They showed that the two individual moduli could complement each other in a hybrid structure yielding an ideal isotropic unit cell with high Young's, shear, and bulk moduli. White et al. [21] used the concept of multi-body interpenetrating lattices where two or more lattices intertwine through the same volume without any direct connection to each other to create a composite-like structure but made of the same constituent material. These previous studies shed light on the importance of studying multi-morphology lattices for different applications.

Computationally, numerical simulations enable detailed deformation analysis of lattices and allow predicting their mechanical and physical properties [24–26]. Several material models and simulation approaches have been investigated recently for sheet-based TPMS lattices. Some studies have focused only on the elastic properties of TPMS-sheet lattices [14,27], while other studies used elastic-ideal plastic constitutive models [28–33]. A few studies have used more complex constitutive models to study the deformation behaviour of TPMS-based lattices at large strains. For example, the plastic model within the finite element analysis (FEA) package Abaqus with isotropic hardening was used to capture the post-yield properties of sheet-networks lattices [32]. The thickness of sheets was adjusted to achieve a good correlation with experimental data. Abueidda et al. [12,34] used the Arruda-Boyce model, an elastic-viscoplastic constitutive model [35] and the flow evolution network (FEN) model and a hyperelastic-viscoplastic model [36] to investigate the mechanical properties of polymeric sheet-networks TPMS lattices. Despite their robustness, the simulations were conducted on a few unit cells only due to their computational cost and could not capture the entire behaviour until densification. Abu Ali et al. [37] also used the FEN model to investigate the mechanical properties of sheet-based TPMS lattices up to 17% strain. The computational simulations results showed good agreement with experimental evidence at low relative densities, while it overestimated the properties at high relative densities. The computational model with unit-cell approach and periodic boundary conditions was also used to determine the yield strength and energy absorption of shell lattices under limited strains [38,39]. Most of the computational studies of sheet-based TPMS lattices analyse their behaviour only at lower strains, e.g. to investigate elastic properties and yield strength [38]. Only a few studies are concerned with TPMS lattices' behaviour up to the densification using solid finite elements (FE), which consume enormous computational time and resources [39].

This work aims to (1) investigate the mechanical properties of multi-morphology (hybrid) lattices with spatially variable cell types designed based on implicit functions, and (2) utilise and validate computational models using shell elements in order to decrease the computational costs. The new computational models can be used to evaluate other designs of implicit functions-based lattices and their crashworthiness performance and increased energy absorption capacity.

2. Methods

2.1. *Geometry and fabrication of specimens*

First, uniform lattices were designed for the purpose of experimental testing and validation of the material model. Two different lattices were considered in this work: Schwarz Diamond and Schoen Gyroid. The lattices were designed and generated using the in-house developed software MSLattice [40]. Each of the analysed lattices was designed with three relative densities ~16%, ~19%, and ~21%. The generated geometries are shown in Fig. 1.

The hybrid TPMS lattices were computer designed, computationally evaluated, fabricated and experimentally tested. The samples are a combination of Gyroid and Diamond lattices in longitudinal and radial loading direction with 16% relative density. The mathematical-based design procedure is described in [40], and the mathematical implementation is explained in details in Appendix 1. Figure 2 shows the CAD generated designs and 3D printed samples.

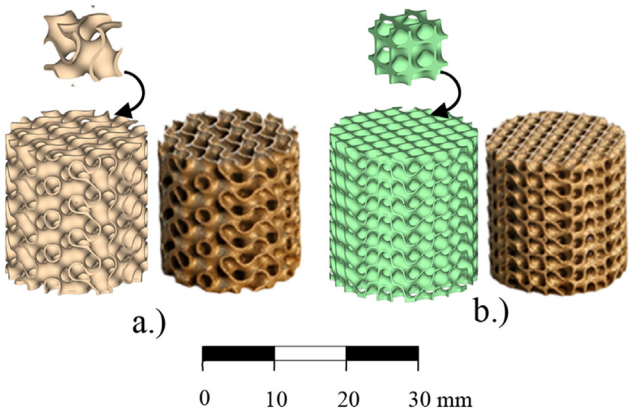

Fig. 1 – Computer-aided design models of the sheet-based TPMS lattices and additively-manufactured samples: Schwarz Diamond, b) Schoen Gyroid.

2.2. *Sample fabrication*

The generated lattices shown in Figs. 1 and 2 were fabricated using the powder bed fusion system EOS M280. The additive manufacturing machine uses a 400W Ytterbium fibre laser with a beam diameter between 100 μm and 500 μm, and a scan speeds up to 7 m/s. Gas atomised stainless steel 316L powder was used to fabricate the plate samples with consistent and repeatable geometry [41].

The fabricated sample plates were blasted with high-pressure air to remove the surrounding residual powder. The final testing samples with dimensions of ∅20 mm × 20 mm were cut from the fabricated plates using the electric wire discharge system. The samples were weighed, and the actual relative densities were calculated in the range of 15%–21.9%. As-built samples show a minor deviation of relative density from the CAD design. The deviation was 4–6% without a clear trend in relation to the relative density. This deviation is attributed to the combination of defects in density and partial adhesion of powder to the surfaces. Five specimens of each lattice group were fabricated and tested.

2.3. *Experimental testing*

Uniaxial compression tests following the standard ISO 13314:2011 [42] were performed by using a servo-hydraulic INSTRON 8801 testing machine with the position-controlled cross-head rate of 0.1 mm/s. The testing conditions were the same for all analysed groups of specimens. The recorded load–displacement data were converted to engineering stress–strain data, using the initial specimen's dimensions. The samples shown in Fig. 1 were tested in previous work [41], and the results are used only for the validation of the computational model. The samples shown in Fig. 2 were developed and tested in this work. The plateau stress was calculated as average stress in the range of 20–40% compressive strain [42], while the specific energy absorption (SEA) was calculated with the integration of compression response up to 40% strain and divided by the density of specimens.

Additionally, the deformation behaviour was evaluated using infrared (IR) thermography, where loading velocity was increased to 284 mm/s to increase IR deformation signature. The Flir SC 5000 high-speed cooled middle-wave IR thermal camera (frame rate 608 Hz with 0.02 K sensitive cooled middle-wave InSb detector) was used for IR thermography to observe the evolution of plastic deformation of specimens during dynamic compression testing. This approach has proved to be sufficient to determine crushing deformation patterns in different cellular materials subject to complex loading conditions [43,44] and proves to be a reliable tool for the validation of computational models [6].

The stress–strain responses of the analysed specimens are shown in Section 3, where the experimental and computational results are compared. Only the average relationships for each group of specimens are plotted since the responses' difference was negligible. The standard deviation values for plateau stress and SEA, which are deducted from stress–strain responses and provided in [41], confirm very high results reproducibility.

2.4. *Computational modelling*

The computational models of TPMS lattices were generated using the shell finite elements (FE) using the own MSLattice code to generate the fundamental lattice geometry of TMPS samples [40]. Meshing was performed by the PrePoMax v1.0.0 software [45], and the boundary conditions were defined in the LS-PrePost software. The manufacturing imperfections resulting in plate thickness variation analysed in our previous work [41] were considered indirectly through the used material parameters determined by inverse parametric

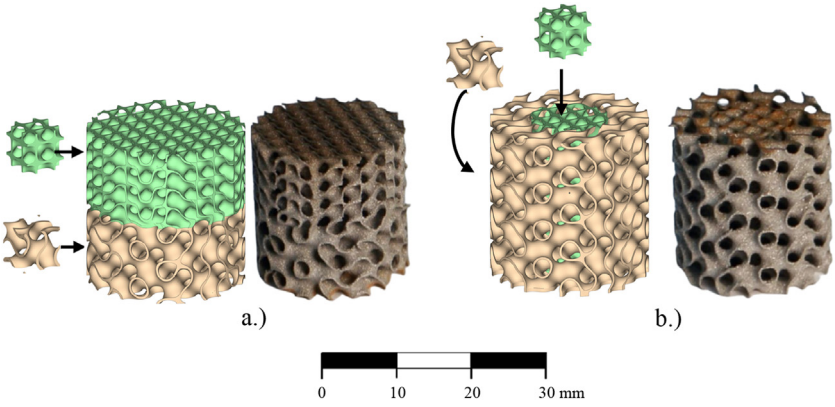

Fig. 2 – Computer model and fabricated specimens of (a) longitudinal and (b) radial hybrid TPMS lattices.

computational simulations. The explicit solver of the LS-DYNA finite element software system [46] was used for all reported computer simulations.

2.4.1. *Material model*

The elastoplastic material model (MAT_024) was used to describe the base material's constitutive behaviour of the analysed TPMS lattices [46]. The model is a rate-dependent, three-piecewise-linear elastic-ideal plastic model [47]. Inverse computational simulations of loaded samples were performed to retrieve the same macroscopic simulation results as those measured in experimental testing for all TPMS geometries and an entire range of strains up to densification. The material parameters of the material model MAT_024 are given in Table 1. The values of yield stresses for AISI 361L are similar to those reported in [48], where the material parameters were determined using different standard tensile and shear specimens. The parameters for the material model are as follows: density ρ, Young's modulus E, Poisson's ratio ν, initial yield stress σ_{yield}, the definition of linear hardening with the second point in the stress–strain diagram (σ_2, $\varepsilon_{pl,2}$). Ideal plasticity after the $\varepsilon_{pl,2}$ was assumed to avoid non-physical removal of FE in the case of considered failure.

The top and bottom compression plates were modelled as linear-elastic (material model MAT_ELASTIC) with the following material parameters: density $\rho = 7850$ kg/m^3, Young's modulus $E = 210$ GPa and the Poisson's ratio $\nu = 0.3$.

2.4.2. *Boundary conditions and finite element mesh*

Fully integrated shell finite elements with two through-thickness integration points were used to discretise the specimens' geometry. The mesh sensitivity analysis was performed with three different FE meshes and three different numbers of through-thickness integration points. The approximate global size of FE was 0.25 mm, which results in approx. 90,000 FE for each lattice. The Belytschko-Tsay shell FE with two through-thickness integration points and the thickness of 1 mm was used to model the compression plates [46].

The following boundary conditions were used: the bottom compression plate with all degrees of freedom fixed, the top compression plate with prescribed constant velocity (2 m/s) towards the bottom plate to speed up the computation time (Fig. 3). The increase in quasi-static testing velocity (from 0.1 mm/s to 2 m/s) was confirmed as acceptable by parametric computational analysis, where the reaction forces on the bottom and upper plate were compared at different loading velocities.

The penalty based node to surface contact formulation with friction was defined between plates and the cellular structure, while the general contact with friction was defined between the TPMS cellular structure plates (shell FE). The coefficient of friction was set to 0.36 and 0.34 for static and dynamic case, respectively. The latter was slightly lower to account for the sliding conditions.

Table 1 – The MAT_024 material model parameters.

ρ [kg/m^3]	E [MPa]	ν [-]	σ_{yield} [MPa]	σ_2 [MPa]	$\varepsilon_{pl,2}$ [-]
7850	210,000	0.3	450	650	0.3

The average thickness of shell FE in computational models was determined using weight comparison between the CAD model, fabricated specimens (micro-computed tomography), and discretised computational models.

3. Computational simulations of TMPS lattices and results validation

The computational results of the constituent TMPS lattices were compared to quasi-static experimental data from [41] for each analysed geometry and relative density in mechanical response (stress–strain relationships) and deformation behaviour. The computational models' deformation behaviour was validated with experimental observations recorded by IR thermography and HD video camera.

3.1. *Diamond TMPS lattice*

The experimental and computational stress–strain relationships of Diamond TPMS lattices with different relative densities are shown in Fig. 4. The overall response is quite comparable, where a typical response of cellular material is observed in experimental in computational results. Experimentally, the slope of the plateau stress increases with increasing the relative density. This is due to the local densification that takes place at earlier strain values in larger relative densities. Computational results show flat plateau stress until a strain value of around 35%, after which plateau will start to increase. The densification is captured well enough by the model. The results are further discussed in detail in Section 3.2.

Computationally and experimentally observed deformation behaviours are shown in Fig. 5. An excellent correlation of the highest plastic strain can be observed for the lowest and highest analysed relative density. The computational results offer a very precise analysis of deformation behaviour, where it can be observed that the layers of unit cells on top and bottom are collapsing first due to boundary effects. After that, the deformation is localised on one side of the specimens and propagates through the structure with increasing global deformation. The deformation is more localised in samples with lower relative densities, which results in limited transverse deformation of the structure. The surfaces of the lattices with lower relative densities can buckle and deform in smaller areas and therefore provide more local deformation. The location of the local deformation is influenced by the fabrication defects, which have a larger influence on the mechanical and deformation behaviour at lower relative densities. The deformation is less localised for higher relative densities, which results in more significant transverse deformation of the structure.

3.2. *Gyroid TMPS lattice*

The computational and experimental mechanical response of Gyroid TPMS lattices with different relative densities is shown in Fig. 6. Experimentally, the plateau stress is almost flat until a strain value of 35% where the effect of local densification starts to become apparent, and the slope of the plateau starts

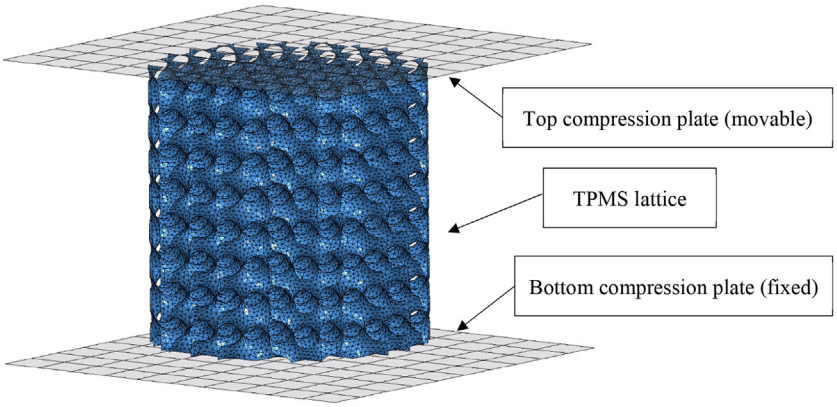

Fig. 3 – Computational model of TPMS lattice.

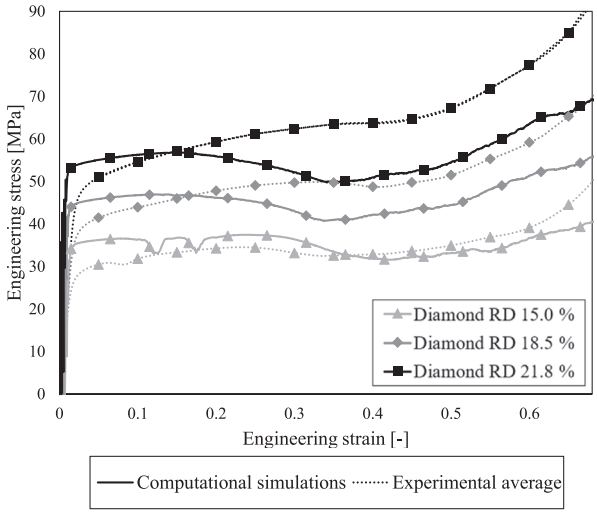

Fig. 4 – Comparison of computational and experimental results for Diamond TPMS lattices with different relative densities.

increasing. The computationally predicted mechanical response shows a more pronounced stress drop in the plateau region and takes place at an earlier strain level (25%–29%). The stress drop is caused by the collapse of one layer of unit cells in the lattice. The stress is more pronounced in the case of the computational model since it's geometry is ideal, and the deformation is more localised as in the case of experiments, where already some parts of other cells fails before and the deformation is not so localised. Overall, a good correlation can be deduced. A higher discrepancy of results is again evident for higher relative densities, which will be discussed in Section 3.2. The model captures the structure densification well.

Very accurate deformation behaviour is captured in the computational model compared to the IR thermography recordings, as shown in Fig. 7. The deformation is localised in the centre of the structure and then spreads to the boundaries with increasing global deformation.

3.3. *Results analysis*

Expected mechanical response of cellular lattices was observed in all analysed samples, where the initial elastic area

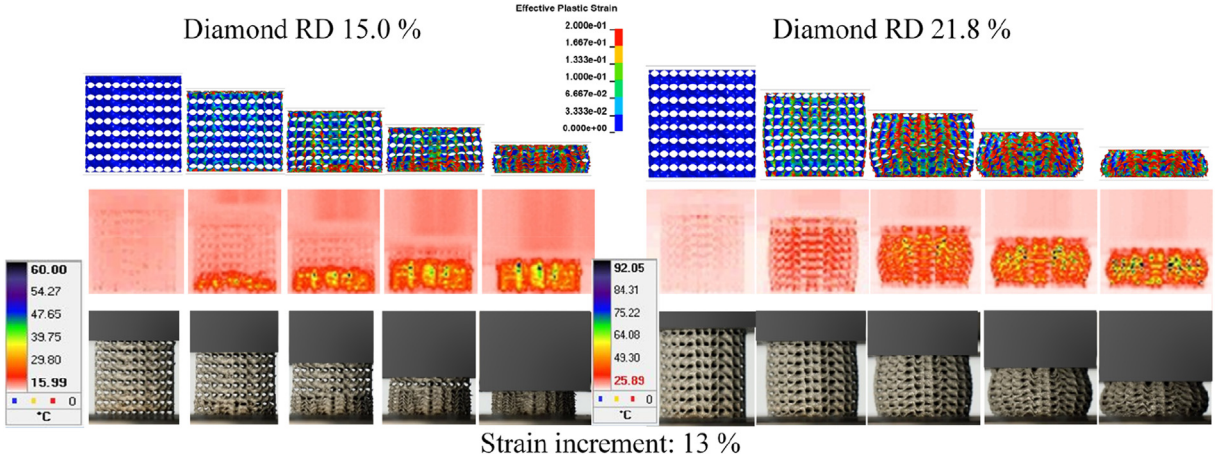

Fig. 5 – Deformation behaviour of Diamond TPMS lattices with the lowest and highest relative density (top to bottom: computational simulations, IR thermography and video sequences of experimental testing).

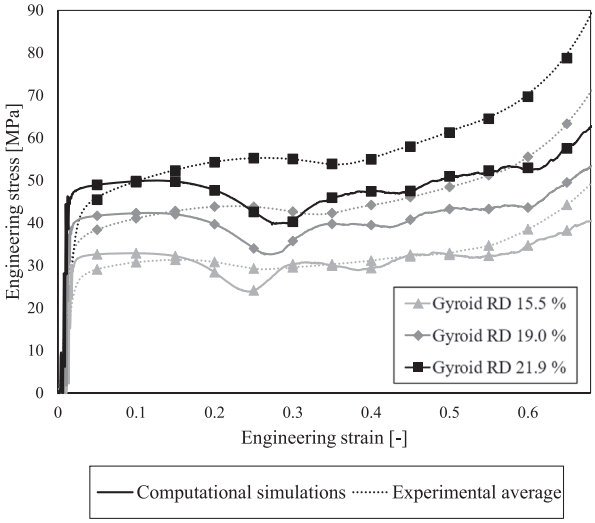

Fig. 6 – Comparison of computational and experimental results for Gyroid TPMS lattices with different relative densities.

is accompanied by substantial plateau stress and final structure densification. The observed responses reveal a smooth transition from elastic to plastic region in all samples, which is a characteristic of sheet-based TPMS lattices.

The robustness of the computational model is evaluated in terms of capturing the plateau stress (average 20–40% strain) and SEA (up to 40% strain) in comparison to the experimental results in Tables 2 and 3.

The plateau stresses and SEA are in most cases underestimated in the computational models up to 24% error which takes place at the highest relative density of the tested Gyroid samples. The results are generally computationally overestimated for lower relative densities in the case of the Diamond and underestimated in the case of the Gyroid. For high relative densities, the computational results are always underestimated compared to experimental values. The results discrepancy originates from internal defects, e.g. micro-voids and micro-cracks, which have a stronger influence in structures with low relative densities. These defects reduce the sheets' load-bearing capacity, showing lower values of mechanical properties compared to the computational model that assumes an ideal, defect-free material. The micro defects have a lower influence in samples with higher relative densities due to the smaller relative size of defects compared to the sheet thickness, leading to better load-bearing capacity.

The difference between the computational and experimental results and the possibility of capturing the correct densification strain is also related to the use of shell finite elements in discretising the geometry. It should be noted that the sheet-based TPMS lattice model used to fabricate the samples and conduct the experiments has been designed using level-set approximation equations. The minimal surface was designed at two iso-values, which define the smooth sheet geometry between them [15,40]. However, a thickening procedure involving offsetting the mid surface in both normal directions to define a shell thickness in building the FE model yields a slightly different structure geometry. This is illustrated in Fig. 8, where the two thickening procedures are visualised. At low relative densities, both thickening procedures yield almost identical geometries. However, at large relative densities, e.g. 50% relative density, the difference becomes more noticeable. This was also observed in other authors' studies that used the volume FE to discretise the TMPS lattice models [32,49]. The use of solid finite elements to discretise the TMPS lattice geometry results in more accurate geometry representation and hence better description of densification but at the expense of very long computational times.

It should be noted that the shell FE are not suitable for very high relative densities (above 50%), where the walls become too thick, and the geometry representation becomes unrealistic. In that case, the thick shell formulation [46] can be used and will be studied in further work. In this study, the results showed that the relative densities in a range of 15–20% were best represented by the computational model using the shell FE.

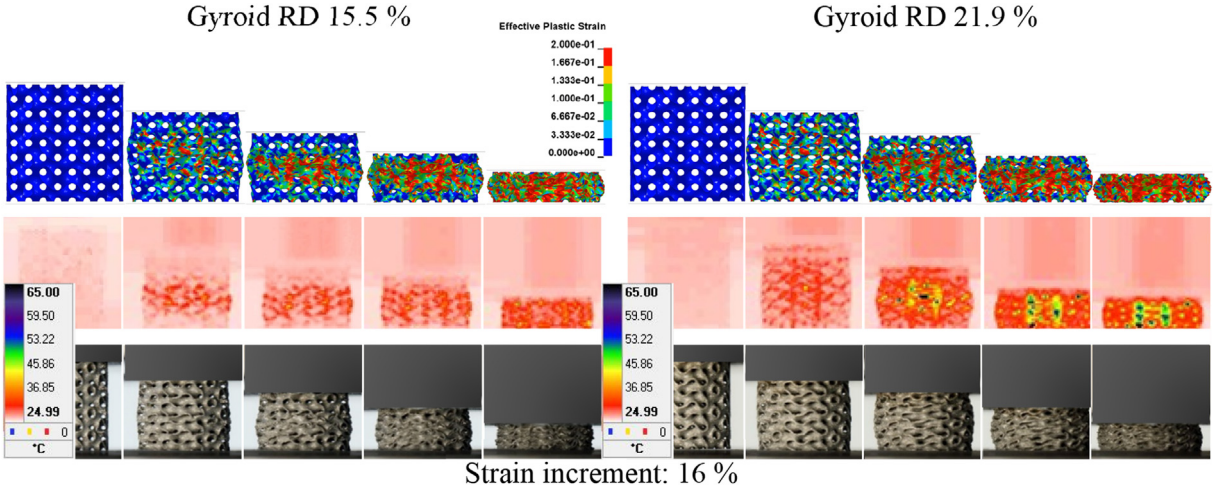

Fig. 7 – Deformation behaviour of Gyroid TPMS lattices with the lowest and highest relative density (top to bottom: computational simulations, IR thermography and video sequences of experimental testing).

Table 2 – Plateau stress and SEA for the TPMS lattices with different relative densities.

Geometry	Relative density [%]	Plateau stress [MPa]			SEA [J/g]		
		Experiment	Simulations	Difference [%]	Experiment	Simulations	Difference [%]
Diamond	15.0	33.39	36.05	7	10.80	11.61	7
	18.5	49.29	44.12	−12	12.47	11.87	−5
	21.8	62.35	53.42	−17	13.25	12.26	−8
Gyroid	15.5	29.99	28.19	−6	9.35	9.10	−3
	19.0	43.18	37.14	−16	10.95	10.01	−9
	21.1	54.68	44.13	−24	11.59	10.38	−12

Table 3 – Plateau stress and SEA for the hybrid and uniform TPMS lattices with 16% relative density.

Geometry	Plateau stress [MPa]			SEA [J/g]		
	Experiment	Simulations	Difference [%]	Experiment	Simulations	Difference [%]
Diamond	33.39	36.05	7	10.80	11.61	7
Gyroid	29.99	28.19	−6	9.35	9.1	−3
Longitudinal Hybrid	37.17	29.51	−22	10.28	8.25	−20
Radial Hybrid	33.53	31.27	−7	9.96	9.27	−7

4. Hybrid TPMS lattice

After validating the computational models for two different fundamental TPMS lattices, the mechanical behaviour of hybrid TPMS lattices was analysed. The experimental tests in this study were performed the same way as for the uniform lattices [41]. The deformation behaviour of the longitudinal and radial hybrid lattices is shown in Fig. 9. In terms of deformation behaviour, an overall good agreement between the experiment and computational simulations can be observed. In longitudinal hybrid samples, the deformation is initiated within the Gyroid lattice, which is less stiff than Diamond lattice (Fig. 9a). While the computational models suggest plastic deformation localisation on the interface between the two lattices, the IR images show evidence of a shear band formation within the Gyroid lattice. The majority of the deformation is taking place in the Gyroid lattice up until 15% strain, after which plastic deformation starts to propagate to the diamond lattice almost uniformly. In the case of radial hybrid lattice, where stiffer Diamond geometry is placed in the centre of lattice and is surrounded radially with the less stiff Gyroid lattice, the deformation is distributed more uniformly. Both computational simulations and IR images

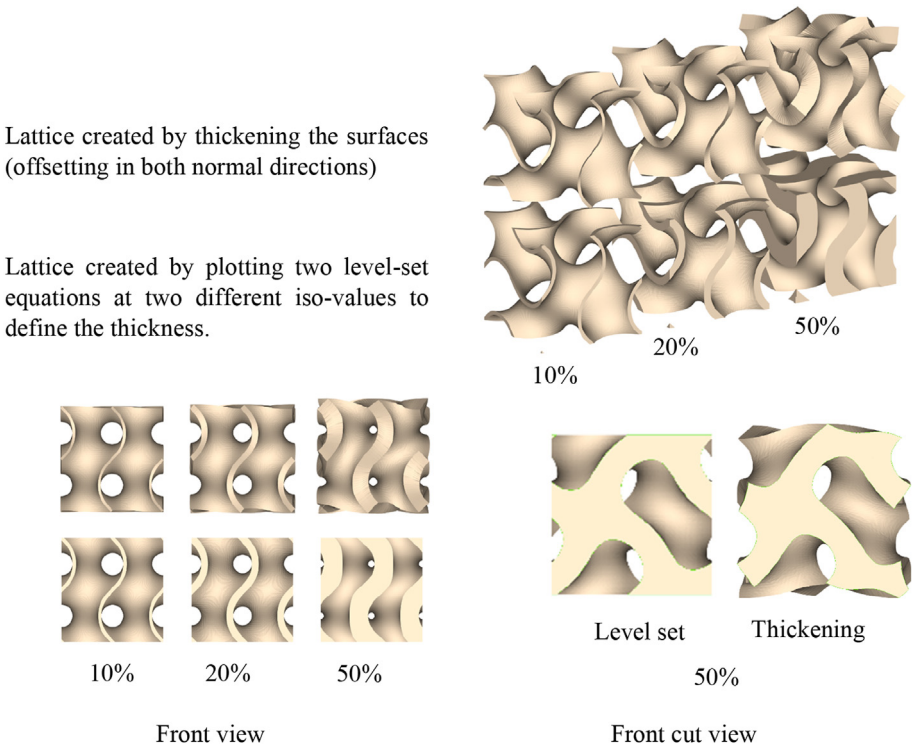

Fig. 8 – Difference between TPMS sheet-lattices obtained through thickening of a shell by offsetting in both normal directions and using level-set equations to define the domain.

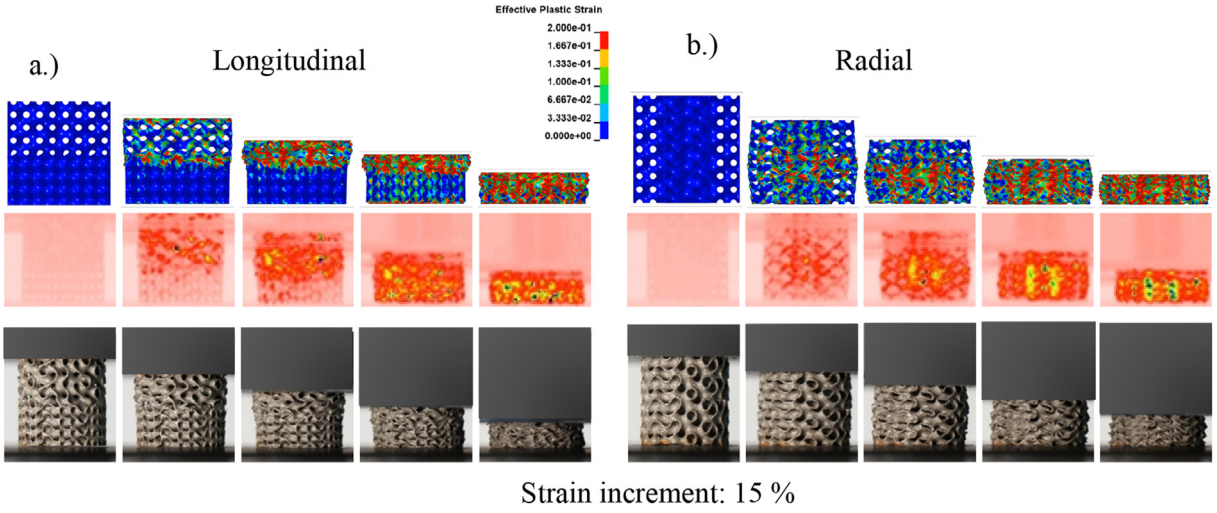

Fig. 9 – Deformation responses of longitudinal (a) and radial (b) hybrid lattices in computational simulations and experiment (IR thermography and video).

suggest stress localisation at the interface between both lattices (Fig. 9b).

The deformation of the radial hybrid lattice was more detailly analysed using the computational simulations, which enabled to plot the plastic strains at different cross-sections of the lattice (Fig. 10). The cross-sections are evenly spaced from the centre of the lattice at a distance of 3.3 mm. The results show that the deformation is more localised in the centre of the specimen built from the Diamond lattice. However, the interface between the two lattice types also shows the stress localisations due to the structure's abrupt stiffness change.

Stress–strain relationships are shown in Fig. 11 for the hybrid as well as uniform lattices for comparison purposes. The longitudinal hybrid lattice response at lower strains is comparable to that those of the uniform Gyroid and uniform Diamond structures. At higher strains, the early densification of the gyroid lattice and the increased contribution of the Diamond lattice drive the plateau stress to increases. This hardening behavior in the plateau region results in higher energy absorption especially beyond the 30% strain level which marks an inflation point where the plateau of the hybrid lattice surpasses that of the diamond lattice. Such behavior can be beneficial in different engineering applications, such as crashworthiness, blast, impact, and ballistic protection. In the case of longitudinal hybrid lattices (Fig. 11a), it can be observed that the simulation response is less stiff than the experimental response, especially at lower strains, which is a consequence of computationally underestimated plateau stresses for Gyroid geometry (Table 2).

The mechanical response of the radial hybrid lattice is shown in Fig. 11b. The plateau stress is much more uniform and constant (flat) than the longitudinal hybrid lattice. The computational and experimental results in the case of radial hybrid lattices are in better correlation than in longitudinal hybrid lattices, which is a consequence of the combined deformation of both lattice geometries. The densification issues in computational models, which were discussed in the previous section, are also present in hybrid lattices.

Comparing the experimental plateau stresses of uniform and longitudinal hybrid structures show up to 19% and 11% enhancement compared to the Gyroid and Diamond structures, respectively. In radial hybrid structures, plateau stress is up to 11% higher than in Gyroid structures and 1% higher than in Diamond structures. The SEA of longitudinal and radial hybrid lattices is 10% and 7% higher than in uniform Gyroid lattice and 5% and 8% lower than in uniform Diamond lattice. A large

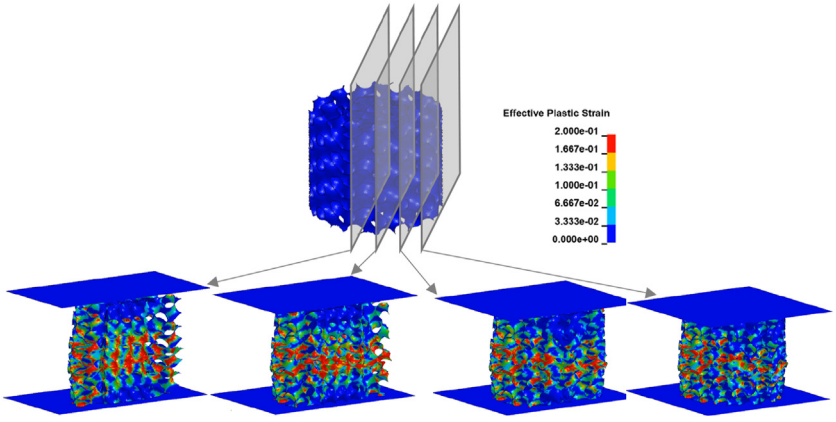

Fig. 10 – Strain distribution at 15% strain in the cross-sections at different depths of the lattice.

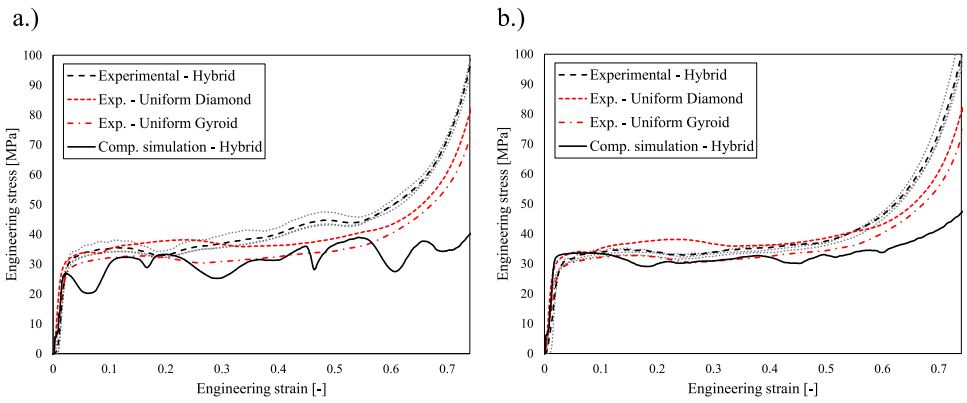

Fig. 11 – Mechanical response of longitudinal (a) and radial (b) hybrid lattices and comparison to computational results.

discrepancy between the computational and experimental results up to 22% underestimation in longitudinal hybrid lattices can be observed, which is attributed to underlying underestimation of the plateau stresses already in the uniform Gyroid lattices as well as observed significant deformation localisation. As shown in Fig. 9a, the deformation localisation at lower strains in the Gyroid lattice is much more pronounced in the simulations than observed in the experiment.

5. Conclusions

In this work, hybrid additively manufactured lattices were investigated for their mechanical behaviour both numerically and experimentally. First, computational models of the TPMS lattices were developed and validated up to the densification strain. The validation of computational models was done using the quasi-static experimental results from previous work [41]. The development of a computational model for explicit LS-DYNA analysis consisted of generating the geometries in MSLattice, meshing in PrePoMax and importing to LS-PrePost, where boundary conditions were defined. The validated computational models can predict the correct deformation behaviour. The computed mechanical responses (stress–strain relationships) are also comparable to experimental results in general. The plateau stress and SEA differ up to 24% and 12%, respectively, for analysed high relative densities. The main reason for the discrepancy is the generation of computational models based on the shell finite element. This could be alleviated by using the volume FE instead of shell FE, which would result in significantly increased computational times and divergence issues for larger deformations. The use of both shell and volume FE leads to delayed densification of the computational model [49]. This study shows that the shell FEs are appropriate for computational simulations of TPMS lattices up to the densification.

Longitudinal and radial hybrid TPMS lattices consisting of Diamond and Gyroid lattices were then developed, fabricated and evaluated using both experiments and computational simulations. Longitudinal hybrid lattices exhibit an inclined plateau region with hardening behaviour due to consecutive deformation and densification of the less stiff Gyroid lattice in a layer-wise manner first followed by more controlled deformation and densification of stiffer Diamond lattice next. The plateau stress in radial hybrid lattices is much more uniform and constant due to the concurrent deformation of radially spaced lattices. The plateau region with progressive characteristic (longitudinal hybrid) and constant characteristic (radial hybrid) can be achieved using the hybrid lattices. Such properties can be beneficial in different engineering applications, e.g. crashworthiness, blast, impact and ballistic protection.

Declaration of Competing Interest

The authors declare that they have no known competing financial interests or personal relationships that could have appeared to influence the work reported in this paper.

Acknowledgements

The authors acknowledge the financial support from the Slovenian Research Agency (fundamental postdoctoral research project (No. Z2-2648) and national research programme funding (No. P2-0063)). This research was partially carried out using the Core Technology Platforms resources at New York University Abu Dhabi.

APPENDIX 1

To design a hybrid cellular material, the design space is split into subdomains using control points. This allows assigning different level-set equations to different subdomains. Mathematically, the level-set equation is described as a weighted sum of the different subdomains:

$$\varphi_{\text{Multi-Morphology}}(x) = \sum_{i=1}^{n} w_i(x) \cdot \varphi_i(x) \quad (1)$$

where the weight functions $w_i(x)$ are defined by:

$$w_i(x) = \frac{1 + \exp(k(\,\|\, x - x_i\|^2)}{\sum_{j=1}^{n} 1 + \exp(k(\,\|\, x - x_j\|^2)} \quad (2)$$

where points $x_i$lay in the ith sub-domain, the ith substructure φ_i is assigned to the ith sub-domain, $n$is the number of control points, andxdenotes the 3D spatial coordinates (x, y, z).

$$\varphi_{Gyroid-Diamond} = \frac{\left(1+e^{(-5+z)^2}\right)\left(\cos\left[2\pi x/5\right]\cos\left[2\pi y/5\right]\cos\left[2\pi z/5\right]+\sin\left[2\pi x/5\right]\sin\left[2\pi y/5\right]\sin\left[2\pi z/5\right]\right)}{2+e^{(-5+z)^2}+e^{(5+z)^2}}+ \frac{\left(1+e^{(5+z)^2}\right)\left(\cos\left[2\pi y/5\right]\sin\left[2\pi x/5\right]+\cos\left[2\pi z/5\right]\sin\left[2\pi y/5\right]+\cos\left[2\pi x/5\right]\sin\left[2\pi z/5\right]\right)}{2+e^{(-5+z)^2}+e^{(5+z)^2}}$$

For example, for the longitudinally graded Gyroid-Diamond hybrid lattice investigated in this study, the following procedure was followed.

1 Defining the constants and level set equations.

$l=5,\ k=0.1,\ p_1=(0,0,5)\ ,p_2=(0,0,-5)$

$\varphi_1=\cos 2\pi x\cos 2\pi y\cos 2\pi z-\sin 2\pi x\sin 2\pi y\sin 2\pi z$

$\varphi_2=\sin 2\pi x\cos 2\pi y+\sin 2\pi y\cos 2\pi z+\sin 2\pi z\cos 2\pi x$

2 Substituting p_1, $p_2$and $k$in the denominator of eq (1) yields:

$$\text{denominator}=2+e^{(-5+z)^2}+e^{(5+z)^2}$$

3 Substituting part 2, and part 3 in eq (2) yields:

4 The equation is inserted in the implicit function tab of the MSLattice software [40] and the isosurface is plotted as shown in Figure A1.

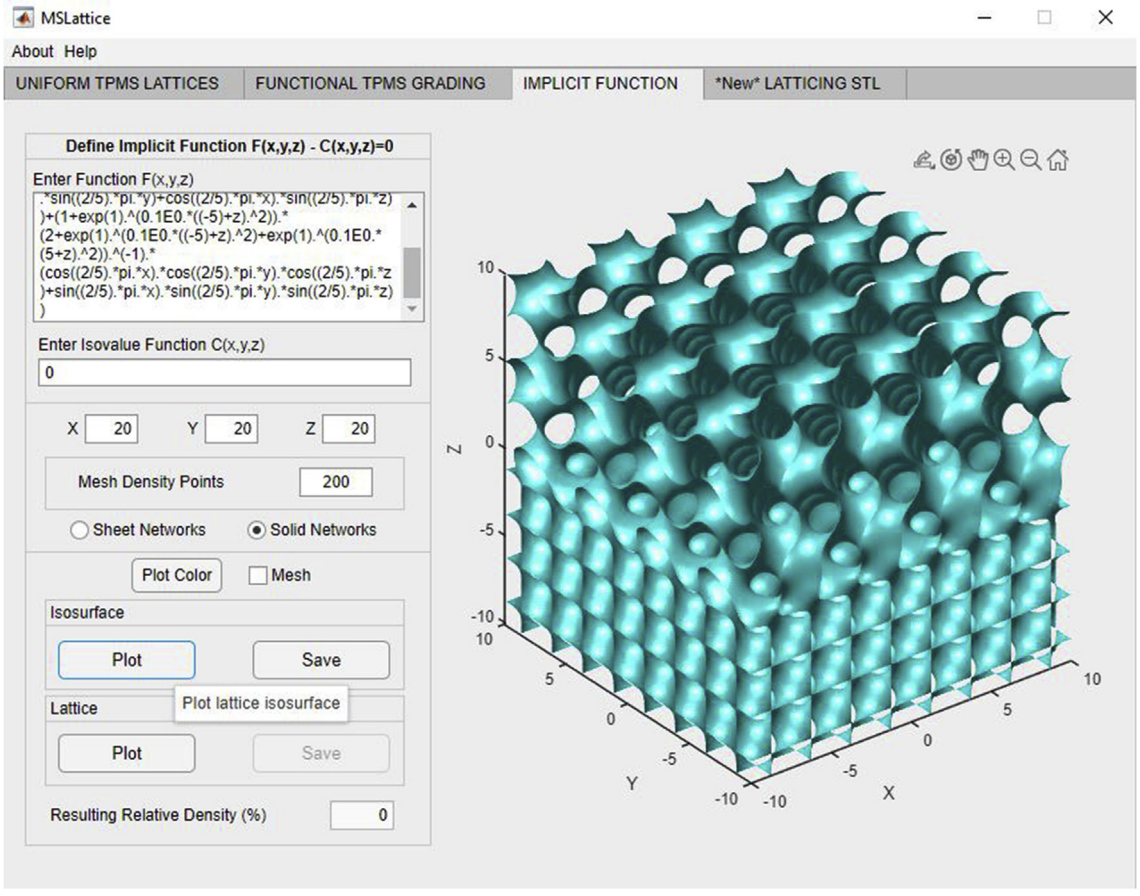

Figure A.1: Creating the hybrid iso-surface in MSLattice.

REFERENCES

[1] Gibson LJ, Ashby MF. Cellular solids: structure and properties. Cambridge, U.K.: Cambridge University Press; 1997.

[2] Ashby MF, Evans A, Fleck NA, Gibson LJ, Hutchinson JW, Wadley HNG. Metal foams: a design guide. Burlington, MA, Massachusetts: Elsevier Science; 2000. https://doi.org/10.1016/S0261-3069(01)00049-8.

[3] Lehmhus D, Vesenjak M, de Schampheleire S, Fiedler T. From stochastic foam to designed structure: balancing cost and performance of cellular metals. Materials 2017;10:1–32. https://doi.org/10.3390/ma10080922.

[4] Rahmani R, Antonov M, Brojan M. Lightweight 3D printed Ti6Al4V-AlSi10Mg hybrid composite for impact resistance and armor piercing shielding. J Mater Res Technol 2020;9:13842–54. https://doi.org/10.1016/j.jmrt.2020.09.108.

[5] Körner C. Additive manufacturing of metallic components by selective electron beam melting — a review. Int Mater Rev 2016;61:361–77. https://doi.org/10.1080/09506608.2016.1176289.

[6] Novak N, Vesenjak M, Krstulović-Opara L, Ren Z. Mechanical characterisation of auxetic cellular structures built from inverted tetrapods. Compos Struct 2018;196:96–107. https://doi.org/10.1016/j.compstruct.2018.05.024.

[7] Al-Ketan O, Rowshan R, Abu Al-Rub RK. Topology-mechanical property relationship of 3D printed strut, skeletal, and sheet based periodic metallic cellular materials. Addit Manuf 2018;19. https://doi.org/10.1016/j.addma.2017.12.006.

[8] Bai L, Gong C, Chen X, Sun Y, Xin L, Pu H, et al. Mechanical properties and energy absorption capabilities of functionally graded lattice structures: experiments and simulations. Int J Mech Sci 2020;182:105735. https://doi.org/10.1016/j.ijmecsci.2020.105735.

[9] Berger JB, Wadley HNG, McMeeking RM. Mechanical metamaterials at the theoretical limit of isotropic elastic stiffness. Nature 2017;543:533–7. https://doi.org/10.1038/nature21075.

[10] Tancogne-Dejean T, Li X, Diamantopoulou M, Roth CC, Mohr D. High strain rate response of additively-manufactured plate-lattices: experiments and modeling. J Dyn Behav Mater 2019;5:361–75. https://doi.org/10.1007/s40870-019-00219-6.

[11] Crook C, Bauer J, Guell Izard A, Santos de Oliveira C, Martins de Souza e Silva J, Berger JB, et al. Plate-nanolattices at the theoretical limit of stiffness and strength. Nat Commun 2020;11:1579. https://doi.org/10.1038/s41467-020-15434-2.

[12] Abueidda DW, Bakir M, Abu Al-Rub RK, Bergström JS, Sobh NA, Jasiuk I. Mechanical properties of 3D printed polymeric cellular materials with triply periodic minimal surface architectures. Mater Des 2017;122:255–67. https://doi.org/10.1016/j.matdes.2017.03.018.

[13] Alhammadi A, Khan KA, Al-Ketan O, Ali MIH, Rowshan R, Abu Al-Rub RK. Microstructural characterization and thermomechanical behavior of additively manufactured AlSi10Mg material and architected cellular structures. 2020. https://doi.org/10.1007/978-3-030-36296-6_15.

[14] Abueidda DW, Abu Al-Rub RK, Dalaq AS, Lee D-W, Khan KA, Jasiuk I. Effective conductivities and elastic moduli of novel foams with triply periodic minimal surfaces. Mech Mater 2016;95:102–15. https://doi.org/10.1016/j.mechmat.2016.01.004.

[15] Al-Ketan O, Abu Al-Rub RK. Multifunctional mechanical metamaterials based on triply periodic minimal surface lattices. Adv Eng Mater 2019;21. https://doi.org/10.1002/adem.201900524.

[16] Al-Ketan O, Rowshan R, Palazotto AN, Abu Al-Rub RK. On mechanical properties of cellular steel solids with shell-like periodic architectures fabricated by selective laser sintering. J Eng Mater Technol 2019;141. https://doi.org/10.1115/1.4041874.

[17] Alhammadi A, Al-Ketan O, Khan KA, Ali M, Rowshan R, Abu Al-Rub RK. Microstructural characterisation and thermomechanical behavior of additively manufactured AlSi10Mg sheet cellular materials. Mater Sci Eng 2020;791:139714. https://doi.org/10.1016/j.msea.2020.139714.

[18] Al-Ketan O, Lee D-W, Rowshan R, Abu Al-Rub RK. Functionally graded and multi-morphology sheet TPMS lattices: design, manufacturing, and mechanical properties. J Mech Behav Biomed Mater 2020;102:103520. https://doi.org/10.1016/j.jmbbm.2019.103520.

[19] Maskery I, Ashcroft IA. The deformation and elastic anisotropy of a new gyroid-based honeycomb made by laser sintering. Addit Manuf 2020;36:101548. https://doi.org/10.1016/j.addma.2020.101548.

[20] Alberdi R, Dingreville R, Robbins J, Walsh T, White BC, Jared B, et al. Multi-morphology lattices lead to improved plastic energy absorption. Mater Des 2020;194:108883. https://doi.org/10.1016/j.matdes.2020.108883.

[21] White BC, Garland A, Alberdi R, Boyce BL. Interpenetrating lattices with enhanced mechanical functionality. Addit Manuf 2021;38:101741. https://doi.org/10.1016/j.addma.2020.101741.

[22] Chen Z, Xie YM, Wu X, Wang Z, Li Q, Zhou S. On hybrid cellular materials based on triply periodic minimal surfaces with extreme mechanical properties. Mater Des 2019;183:108109. https://doi.org/10.1016/j.matdes.2019.108109.

[23] Jia H, Lei H, Wang P, Meng J, Li C, Zhou H, et al. An experimental and numerical investigation of compressive response of designed Schwarz Primitive triply periodic minimal surface with non-uniform shell thickness. Extrem Mech Lett 2020;37:100671. https://doi.org/10.1016/j.eml.2020.100671.

[24] Novak N, Borovinšek M, Vesenjak M, Wormser M, Körner C, Tanaka S, et al. Crushing behavior of graded auxetic structures built from inverted tetrapods under impact. Phys Status Solidi B 2018;256:1–7. https://doi.org/10.1002/pssb.201800040.

[25] Vesenjak M, Veyhl C, Fiedler T. Analysis of anisotropy and strain rate sensitivity of open-cell metal foam. Mater Sci Eng 2012;541:105–9. https://doi.org/10.1016/j.msea.2012.02.010.

[26] Imbalzano G, Tran P, Ngo TD, Lee PVS. A numerical study of auxetic composite panels under blast loadings. Compos Struct 2015;135:339–52. https://doi.org/10.1016/j.compstruct.2015.09.038.

[27] Dalaq AS, Abueidda DW, Abu Al-Rub RK, Jasiuk IM. Finite element prediction of effective elastic properties of interpenetrating phase composites with architectured 3D sheet reinforcements. Int J Solid Struct 2016;83:169–82. https://doi.org/10.1016/j.ijsolstr.2016.01.011.

[28] Montazerian H, Davoodi E, Asadi-Eydivand M, Kadkhodapour J, Solati-Hashjin M. Porous scaffold internal architecture design based on minimal surfaces: a compromise between permeability and elastic properties. Mater Des 2017;126:98–114. https://doi.org/10.1016/j.matdes.2017.04.009.

[29] Afshar M, Pourkamali Anaraki A, Montazerian H. Compressive characteristics of radially graded porosity scaffolds architectured with minimal surfaces. Mater Sci Eng C 2018;92:254–67. https://doi.org/10.1016/j.msec.2018.06.051.

[30] Al-Ketan O, Abu Al-Rub RK, Rowshan R. The effect of architecture on the mechanical properties of cellular

structures based on the IWP minimal surface. J Mater Res 2018;33. https://doi.org/10.1557/jmr.2018.1.
[31] Al-Ketan O, Rezgui R, Rowshan R, Du H, Fang NX, Abu Al-Rub RK. Microarchitected stretching-dominated mechanical metamaterials with minimal surface topologies. Adv Eng Mater 2018;20:1800029. https://doi.org/10.1002/adem.201800029.
[32] Zhang L, Feih S, Daynes S, Chang S, Wang MY, Wei J, et al. Energy absorption characteristics of metallic triply periodic minimal surface sheet structures under compressive loading. Addit Manuf 2018;23:505–15. https://doi.org/10.1016/j.addma.2018.08.007.
[33] Lee MG, Lee JW, Han SC, Kang K. Mechanical analyses of "Shellular", an ultralow-density material. Acta Mater 2016;103:595–607. https://doi.org/https://doi.org/10.1016/j.actamat.2015.10.040.
[34] Abueidda DW, Elhebeary M, Shiang C-S, Pang S, Abu Al-Rub RK, Jasiuk IM. Mechanical properties of 3D printed polymeric Gyroid cellular structures: experimental and finite element study. Mater Des 2019;165:107597. https://doi.org/https://doi.org/10.1016/j.matdes.2019.107597.
[35] Arruda EM, Boyce MC. A three-dimensional constitutive model for the large stretch behavior of rubber elastic materials. J Mech Phys Solid 1993;41:389–412. https://doi.org/10.1016/0022-5096(93)90013-6.
[36] Dreher ML, Nagaraja S, Bergstrom J, Hayman D. Development of a flow evolution network model for the stress–strain behavior of poly(L-lactide). J Biomech Eng 2017;139. https://doi.org/10.1115/1.4037071.
[37] Abou-Ali AM, Al-Ketan O, Lee DW, Rowshan R, Abu Al-Rub RK. Mechanical behavior of polymeric selective laser sintered ligament and sheet based lattices of triply periodic minimal surface architectures. Mater Des 2020;196:109100. https://doi.org/10.1016/j.matdes.2020.109100.
[38] Bonatti C, Mohr D. Mechanical performance of additively-manufactured anisotropic and isotropic smooth shell-lattice materials: simulations & experiments. J Mech Phys Solid 2019;122:1–26. https://doi.org/10.1016/j.jmps.2018.08.022.
[39] Bonatti C, Mohr D. Smooth-shell metamaterials of cubic symmetry: anisotropic elasticity, yield strength and specific energy absorption. Acta Mater 2019;164:301–21. https://doi.org/10.1016/j.actamat.2018.10.034.
[40] Al-Ketan O, Abu Al-Rub RK, MSLattice. A free software for generating uniform and graded lattices based on triply periodic minimal surfaces. Mater Des Proc Commun 2020:1–10. https://doi.org/10.1002/mdp2.205.
[41] Novak N, Al-ketan O, Krstulović-Opara L, Rowshan R, Al-rub RKA, Vesenjak M, et al. Quasi-static and dynamic compressive behaviour of sheet TPMS cellular. Compos Struct 2021;266:113801. https://doi.org/10.1016/j.compstruct.2021.113801.
[42] ISO 13314:2011 - mechanical testing of metals - ductility testing - compression test for porous and cellular metals. Geneva, Switzerland: International Organization for Standardization; 2011. www.iso.org.
[43] Duarte I, Vesenjak M, Krstulović-Opara L, Ren Z. Static and dynamic axial crush performance of in-situ foam-filled tubes. Compos Struct 2015;124:128–39. https://doi.org/10.1016/j.compstruct.2015.01.014.
[44] Vesenjak M, Gačnik F, Krstulović-Opara L, Ren Z. Mechanical properties of advanced pore morphology foam elements. Mech Adv Mater Struct 2015;22:359–66. https://doi.org/10.1080/15376494.2012.736059.
[45] Borovinšek M. PrePoMax, (n.d.). http://lace.fs.uni-mb.si/wordpress/borovinsek/?page_id=41.
[46] Hallquist J. LS-DYNA keyword user's manual. Livermore, California: Livermore Software Technology Corporation; 2007.
[47] Marzi S, Hesebeck O, Brede M, Kleiner F. A rate-dependent , elasto-plastic cohesive zone mixed-mode model for crash analysis of adhesively bonded joints. In: 7th Eur. LS-DYNA conf.,; 2009.
[48] Li X, Roth CC, Tancogne-dejean T, Mohr D. Rate- and temperature-dependent plasticity of additively manufactured stainless steel 316L: characterisation, modeling and application to crushing of shell-lattices. Int J Impact Eng 2020:103671. https://doi.org/10.1016/j.ijimpeng.2020.103671.
[49] Zhou H, Zhao M, Ma Z, Zhang DZ, Fu G. Sheet and network based functionally graded lattice structures manufactured by selective laser melting: design, mechanical properties, and simulation. Int J Mech Sci 2020;175. https://doi.org/10.1016/j.ijmecsci.2020.105480.